Descriptive Analysis of Frontal Symmetric Instabilities without Background Temperature Gradient

Jinxuan Zhu[1] and Baylor Fox-Kemper[1]

[1]*Department of Earth, Environment and Planetary Science, Brown University*

May 19, 2017

We examine the SI effects and Bachman's SI Parameterization in a two-fronts LES simulation. The domain, governed by periodic horizontal temperature profile, consists of a Geostrophic Stable front and a Geostrophic Unstable front. In the study, we find that the Bachman's SI Parameterization is not good enough to reproduce the Reynolds stress and the SI turbulent buoyancy transport in the LES simulation. The Geostrophic Shear Production by the SI eddy effects are not a linear vertical profile but a two stage equation. On the first stage from the surface to a depth about $-15\,\mathrm{m}$, the GSP increases linearly. On the second stage from the depth about $-15\,\mathrm{m}$ to the mixing layer bottom, the GSP decreases linearly. We also find that the Reynolds stress in this simulation consists of not only SI turbulence beyond the horizontal resolution of $10\,\mathrm{m}$, but also averaged LES subgrid friction. The LES subgrid friction is as important as SI turbulent momentum transport in the SI active grids.

1 Introduction

The state-of-art regional models are suffering problems in simulating geostrophic unstable fronts (Smith, Hamlington, and Fox-Kemper 2016; Leif N. Thomas et al. 2013), where wind stress and evaporation moves colder water onto the warmer, and the strong fronts in the climate system are often identified with geostrophic instabilities, including Gulf Stream, Kuroshio and Antarctic Circumpolar Current where wind-driven Ekman transport carries colder water onto the warmer water. For the failure of models, a potential explanation is models' incapacity of simulating Symmetric Instabilities (SI) (B. Hoskins 2015; B. J. Hoskins 1974). SI is a kind of instability by negative potential vorticity (PV) on Northern Hemisphere (or positive in Southern Hemisphere), with turbulences scaling from $10\,\mathrm{m}$ to $100\,\mathrm{m}$ (Stone 1966), of which the models are incapable to resolve.

In recent years, Bachman, Scott et al. (2015) built an experimental SI parameterization in MITgcm, based on theories (Stone 1966) and idealized Large Eddy Simulation (LES) (John R. Taylor and

Ferrari 2010; L. N. Thomas and J. R. Taylor 2010; Leif N. Thomas et al. 2013). However, these studies relies upon an ideal ocean front assuming a constant horizontal temperature gradient and negligible vertical advection, while the assumption could unrealistic for the real ocean front. This study examines the parameterization in a more realistic ocean scenario(Smith, Hamlington, and Fox-Kemper 2016) in which the Symmetric Instabilities is not generated by the background temperature gradient.

Two models will be used in this study, LES and MITgcm. The LES models geostrophic fluid with a resolution of 10 m, a resolution enough to resolve SI turbulence on grids. MITgcm is simulated with a horizontal resolution 100 m, a resolution beyond the SI turbulence but capable of detecting negative PV. MITgcm will be ran with and without Bachman's SI Parameterization to examine the performance of the parameterization. By comparing between LES and parameterized MITgcm results, we find that the SI parameterization is not mature enough for direct deployment in regional ocean studies at this stage.

The paper is planned as follows: Section 2 will introduce the Bachman's SI Parameterization. Section 3 will compare the MITgcm simulations with the LES truth simulation, for examining how well the Bachman's SI parameterization works. Section 4 analyses the Reynolds stress and GSP in the LES simulation, to understand the difference between the Bachman's parameterized SI and the true SI effect of the LES. Section 5 is the conclusion.

2 An Introduction of Bachman SI Parameterization

Here we will provide a brief introduction for Bachman's SI Parameterization.(Bachman, Scott et al. 2015)

The parameterization solves three problems, where SI is activated, how the turbulence viscosity (Reynolds Stress) is changed by SI, how the turbulence diffusivity is changed by SI.

2.1 Where SI is turned on

SI is the turbulences formed by the negative Ertel's PV (B. Hoskins 2015), therefore, in Bachman's SI Parameterization, the SI turbulences is active on the regions of negative PV formation.

MITgcm is governed by

$$\frac{\partial \mathbf{u_h}}{\partial t} + \mathbf{u} \cdot \nabla \mathbf{u_h} + f\mathbf{k} \times \mathbf{u_h} = b\mathbf{k} - \nabla\phi + \mathbf{F} \tag{1}$$

$$\frac{\partial b}{\partial t} + \mathbf{u} \cdot \nabla b = -D \tag{2}$$

$$\nabla \cdot \mathbf{u} = 0 \tag{3}$$

, where $\mathbf{F} = -\partial_j \langle u'_j \mathbf{u_h} \rangle$ is the Reynolds friction, $D = -Q + \partial_j \langle u'_j b \rangle$ indicates the buoyancy change due to the boundary forcing Q and the diffusion $\langle w'b' \rangle$, and $\mathbf{u_h}$ is the horizontal velocity.

From the basic governing equations, we could have the Ertel's Potential Vorticity, calculated by the mean flow, and its tendency by (Shown in Appendix A, or see Leif N. Thomas 2005; Marshall and Nurser 1992)

$$q = \omega_a \cdot \nabla b \tag{4}$$

$$\frac{\partial q}{\partial t} = -\nabla(q\mathbf{u}) - \nabla \mathbf{J} \tag{5}$$

$$\mathbf{J} = -\omega_a D + (\nabla b) \times \mathbf{F}) \tag{6}$$

, where q is the Ertel's Potential Vorticity (PV), and ω_a is the absolute vorticity.

Because SI is associated with negative PV, we choose the SI influenced regions by negative surface PV forcing $J(z=0) < 0$. In (L. N. Thomas and J. R. Taylor 2010), it is found that, at least in an idealized ocean front, the negative PV forcing is generated with geostrophic instability where

$$B_E + B_o \approx -HJ(z=0) > 0 \tag{7}$$

, where H is the scaling of mixing layer depth, $B_E = -\partial \mathbf{u_g} \tau$ is the surface Ekman Buoyancy Transport (EBF), B_o is the surface buoyancy fluxes due to evaporation, precipitation, heating and cooling.

Therefore, in Bachman's SI Parameterization, we choose the SI active region as regions of $B_E + B_o > 0$

2.2 What is the viscosity and diffusion of the SI mixing layer

In SI active region, the surface buoyancy fluxes and the surface wind-stress are transported downward by two different layers(John R. Taylor and Ferrari 2010). The surface buoyancy fluxes transports downward by a non-local convection until the convective layer h_{conv}, and the momentum is transport downward deeper until the Richardson mixing layer h_{ri}.

The Richardson number $Ri = -1$ determines a condition that $q = 0$.(Leif N. Thomas et al. 2013) The Richardson layer depth is determined by where the Richardson number is -1 that

$$\Delta_z b h_{\mathrm{ri}} = (\Delta_z \mathbf{u})^2 \tag{8}$$

, where $\Delta_z x = x(z) - x(z=0)$ is the difference between the surface and the depth.

The non-local buoyancy convection reduces the whole water column beyond the convective layer

3

until the stratification is unchanged between the surface and the depth:

$$\frac{1}{h_{\text{conv}}} \int_{h_{\text{conv}}}^{0} \mathrm{d}z \frac{\partial b}{\partial t} = \frac{1}{h_{\text{ri}} - h_{\text{conv}}} \int_{h_{\text{ri}}}^{h_{\text{conv}}} \mathrm{d}z \frac{\partial b}{\partial t} \tag{9}$$

$$\frac{\partial b}{\partial t} \int_{h_{\text{conv}}}^{0} \mathrm{d}z \frac{\partial b}{\partial t} = B_o - \int_{h_{\text{conv}}}^{0} \mathrm{d}z \nabla(\mathbf{u}b) \tag{10}$$

$$\int_{h_{\text{ri}}}^{h_{\text{conv}}} \mathrm{d}z \frac{\partial b}{\partial t} = - \int_{h_{\text{ri}}}^{h_{\text{conv}}} \mathrm{d}z \nabla(\mathbf{u}b) \tag{11}$$

Based on the analysis in the idealized front (John R. Taylor and Ferrari 2010), the convective layer h_{conv} could be approximated by

$$\left(\frac{h_{\text{conv}}}{h_{\text{ri}}} \right)^4 - c^3 \left(1 - \frac{h_{\text{conv}}}{h_{\text{ri}}} \right)^3 (x)^2 = 0 \tag{12}$$

The viscosity is parameterized by Geostrophic Shear Production (GSP) P_G, and GSP, as argued in John R. Taylor and Ferrari 2010, could be approximated by a linear function thorough z, that

$$P_G + \overline{w'b'} = (B_E + B_o) \frac{z}{h_{ri}} \tag{13}$$

$$\langle w'b' \rangle_{non_local} = B_o \frac{z}{h_{conv}} \tag{14}$$

, where $P_G = - \langle \mathbf{u}'w' \rangle \partial \mathbf{u_g} / \partial z$ is GSP, $\langle w'b' \rangle_{non_local}$ is the non-local turbulence vertical buoyancy transport.

Then the viscosity as a scalar ν and the Reynolds friction in SI effects are parameterized as

$$\nu = \frac{P_G}{(\partial \mathbf{u_g} / \partial z) \cdot (\partial \mathbf{u} / \partial z)} \tag{15}$$

$$\langle \mathbf{u}'w' \rangle = -\nu \frac{\partial \mathbf{u}}{\partial z} \tag{16}$$

And the diffusivity is parameterized with a regressed Prantl number (Bachman, Scott et al. 2015)

$$\kappa = \frac{2\nu}{1 + 10 \max(0, Ri_b)^{0.8}} \tag{17}$$

$$Ri_b = \frac{\partial b / \partial z}{(\partial \mathbf{u_g} / \partial z)^2} \tag{18}$$

$$\langle w'b' \rangle = -\kappa \frac{\partial b}{\partial z} + B_o \frac{z}{h_{conv}} \tag{19}$$

, where the Ri_b is the Geostrophic Balanced Richardson number, $\langle w'b' \rangle$ the turbulence vertical buoyancy includes the local and non-local parts.

4

2.3 A quick lookup

In the Bachman's SI Parameterization, the SI effects are active on regions under the forced geostrophic instability as in Eqn. 7. On these regions, the SI effects are parameterized by two layers, Richardson mixing layer (Eqn. 8) as the whole mixing layer and the convective mixing layer (Eqn. 12) for the non-local turbulence vertical buoyancy transport. The viscosity and the Reynolds' friction stress, based on GSP as in Eqn. 16, are parameterized as in Eqn. 15 and Eqn. 16. The vertical turbulence buoyancy transport and the diffusivity are parameterized as in Eqn. 17 and Eqn. 19.

3 Performance of the Previous Parameterization

3.1 Experiment Setup

Bachman's SI Parameterization has been shown well in simple ideal front scenarios (Bachman, Scott et al. 2015). Generally, in the parameterization studies, the domain is periodic and small, no bigger than $1 \, \text{km} \times 1 \, \text{km}$ horizontally, and SI exists everywhere by a background horizontal temperature gradient. However, the background temperature gradient and a small domain could be unrealistic for the real SI fronts. To simulate the SI effect and examine the SI Parameterization in a more realistic scenario, we want to simulate a domain that

- The domain should be big enough to capture the front structures.

- The domain should be small enough that the LES is capable to simulate with $10 \, \text{m}$ horizontal resolution.

- The front is not sustained by a pre-given background gradient, and the horizontal buoyancy gradient is permitted to change vertically by oceanic processes.

Therefore, the two front periodic domain studied by Hamlington et al. (2014) are used for a more realistic Symmetric Instability simulation. The two fronts domain simulation have been analysed for the interaction between SI and Langmuir turbulence (Hamlington et al. 2014; Suzuki et al. 2016) and for tracers diffusion in SI fronts(Smith, Hamlington, and Fox-Kemper 2016). In this study, we will run 3 simulations to examine Bachman's SI Parameterization

- a LES simulation (LES truth), in which SI effects are perfectly resolved. We will use 'LES truth' to represent this simulation later in this paper.

- a MITgcm simulation without Bachman's SI Parameterization (MITgcm KPP), in which SI effects are not represented. We will use 'MITgcm KPP' to represent this simulation later in this paper.

- a MITgcm simulation with Bachman's SI Parameterization (MITgcm SI), in which SI effects are parameterized based on Bachman, Scott et al. 2015. We will use 'MITgcm SI' to represent this simulation later in this paper.

The experiment parameters and setup are already shown by Hamlington et al. (2014) and Smith, Hamlington, and Fox-Kemper (2016). The LES and MITgcm simulations model the spindown of two fronts forced by wind-stress without surface heat fluxes. No salinity gradient exists, so the buoyancy is subject to the temperature profile. Fig. 1 shows the temperature initialization and the wind-stress forcing. The temperature is initialized with a geostrophic stable front and a geostrophic unstable front, two fronts are as deep as 60 m, a typical mixing layer depth. The wind-stress are constant over time with a 30° aligned to the front, and the amplitude of wind-stress is $\tau_0 = 0.025\,\mathrm{Nm}^-2$. The More details and other parameters could be seen in the Table 1 of Hamlington et al. 2014.

As being periodic, the domain includes a geostrophic stable front and a geostrophic unstable front. The geostrophic unstable front is forced by a positive Ekman Buoyancy Transport, and therefore is the regime of Forced Symmetric Instability as in the Bachman's Parameterization. The geostrophic unstable front is located around $y = 12.5\,\mathrm{km}$ by the initialization, and moves southward by Ekman flow.

3.2   Comparison and Results

We compare the three simulations at the twelfth day after initialization. The initialization is almost homogeneous along the x-axis (aligning the front), so the difference along the x-axis is small and not interesting. Therefore, we will use the surface variabilities, x-averaged variabilities and horizontal averaged variabilities to examine the fronts.

In interpolating the LES results onto the MITgcm grids, a 12 hours average is applied for eliminating the inertia waves of the LES. Variables of u, v, θ, b is interpolated by the volume average of each MITgcm grid. The momentum and buoyancy fluxes like uw, wb and vertical velocity w are interpolated by face average.

Fig. 2 shows the Surface PV and the Surface Sea Temperature (SST) of the three simulations at twelfth day. All three simulations reveals a turbulent geostrophic unstable front around $5\,\mathrm{km} < y < 10\,\mathrm{km}$, and a geostrophic stable front around $15\,\mathrm{km} < y < 20\,\mathrm{km}$. Negative PV is seen at geostrophic unstable fronts in all three simulations. However, the negative PV in LES truth is stronger and more widespread in y-axis than negative PV in MITgcm KPP and MITgcm SI, and the geostrophic unstable front is more turbulent in LES truth than in MITgcm KPP and MITgcm SI. Each of the three simulations shows a geostrophic unstable front and a geostrophic stable front, but the LES has a more turbulent and stronger geostrophic unstable front.

Fig. 3 shows the vertical PV and the vertical temperature difference with x-averaging, and the vertical temperature difference is the potential temperature difference by the SST and the temperature in the depth. It shows that all three simulation have a similar PV mixed layer depth by a benchmark

$q(z) < q_c = 8 \times 10^{-10}\,\text{s}^{-3}$. However, in the first 20 m depth, the PV is distributed differently in LES truth than in MITgcm KPP and MITgcm SI. In the geostrophic unstable front, the negative PV of LES truth is constrained in the layer $z > -10\,\text{m}$, while negative PV of the MITgcm simulations can be as deep as $-20\,\text{m}$. Compared with the PV of MITgcm simulations, the negative PV of the LES truth is distributed more uniformly along y-axis in the geostrophic unstable front.

The vertical temperature profile is also different between LES truth and MITgcm simulations. The MITgcm simulations overestimate the vertical stratification at the boundary layer $z > -60\,\text{m}$. By a benchmark $\Delta\theta > \Delta\theta_c = 2 \times 10^{-3}\,\text{K}$, the temperature mixed layer of the LES truth are about $-20\,\text{m}$ at the geostrophic unstable front, while the mixed layer of MITgcm KPP or MITgcm SI is about $-40\,\text{m}$ at the geostrophic unstable front.

Fig. 4 compares the vertical profile of GSP $P_G = -\langle u'w' \rangle \partial_z u_g$ and the eddy vertical buoyancy transport $w'b'$ averaged in the SI regime defined by $B_E > 0$.

Fig. 4a shows that the GSP is larger in MITgcm simulations than the LES truth, and the GSP are similarly between MITgcm KPP and MITgcm SI. It shows that the SI Parameterization does not have a strong effect on GSP.

Fig. 4b shows the ratio between GSP and EBF between three simulations. In both MITgcm KPP (red line) and MITgcm SI (yellow line), the GSP-EBF ratio could be approximated by a linear function over z like Bachman's SI Parameterization, while the LES truth (blue line) shows a strange vertical GSP profile. The GSP-EBF ratio (blue line in Fig. 4b) in LES truth increases to about 3 around first 15 m, and then dumps linearly to zero. The vertical GSP in the LES truth shows that the GSP could be stronger than EBF in real SI effects, which is different from previous SI studies. Therefore, we could come to two conclusions.

- As the GSP profiles in the MITgcm KPP and MITgcm SI are similar, we could conclusion that in this simulation the SI parameterization is not significantly different from the KPP parameterization in calculating the Reynolds friction stress.

- The GSP profile in the LES truth could not be estimated by the vertical linear function as in the Bachman's parameterization.

Fig. 4c shows the $w'b'$ averaged on all SI active grids, and Fig. 4d shows the $w'b'$ per EBF on all SI active grids. The vertical distribution of the $w'b'$ is different between the LES and MITgcm simulations. Though the amplitudes of $w'b'$ are similar between three simulations, the $w'b'$ as a response to EBF are different between LES and MITgcm simulations. In MITgcm KPP and MITgcm SI, the $w'b'$ is much smaller than EBF, as the ratio varying between -0.2 and 0. On the other hand, the $w'b'$ is comparable with EBF in LES truth, with the ratio varying between -1.0 and 0.2

4 Diagnosing the LES results

In the comparison of the last section, we found that the LES truth differs from the MITgcm SI and MITgcm KPP in PV, temperature, GSP and $w'b'$. In the LES simulation, the geostrophic unstable front is more unstable, and the GSP vertical profile is different from the Bachman's Parameterization.

4.1 Geostrophic Instability and Symmetric Instability

As Sec. 2 shows, the Bachman's SI Parameterization turns on SI parameterization where geostrophic instability is active. This subsection would examine the overlap between the Symmetric Instability (SI) and Geostrophic Instability (GI). Table 1 shows the percentage of grids in LES truth governed by different instability at the twelfth day. It shows a good consistency between SI and GI that most SI influenced grids are captured by the GI prediction, and most GI grids are influenced by SI. Therefore, at least in this simulation, the Bachman's SI parameterization works well on deciding where the SI is active.

Instability	Percentage
GI and SI	35.0 %
GI, no SI	5.0 %
SI, no GI	4.5 %
None	55.5 %
False Positiveness	12.5 %
False Negativeness	7.5 %

Table 1: Percentage of Grids governed by different instability; The Geostrophic Instability (GI) grids are grids where a negative vertical stratification is generated by $B_E + B_O > 0$ as in Eqn. 7. The Symmetric Instability (SI) grids are grids where the surface PV is negative. The False Positiveness is the possibility that falsely predict SI grids by positive GI. The False Negativeness is the possibility that falsely predict no-SI grids by negative GI.

4.2 GSP Profile

Previous studies show that GSP is an important factor in diagnosing the SI effects. And when the domain is periodic or the Rossby number is much smaller than 1, the Ekman and geostrophic balance indicates that the Geostrophic Shear Production plays an important role in the Turbulent Kinetic Energy (TKE).(John R. Taylor and Ferrari 2010) Previous studies find that the GSP in the ideal ocean front scenario is approximately a linear function through z.

In the last section comparing LES and MITgcm simulations, we have found that, on the SI regime, the GSP P_G is not a vertical linear function as discussed in ideal ocean. Fig. 4a shows the GSP

averaged by all SI regions, and how the Reynolds stress aligning or crossing the front contribute to the total GSP. It shows that the GSP P_G is mostly contributed by the friction align the front and the temperature gradient across the front, a consistent result with analysis in previous studies (John R. Taylor and Ferrari 2010). However, the GSP P_G is not a vertical linear function, but two vertical linear functions meeting about $z = -10\,\mathrm{m}$ where the maximum of P_G occurs, as

$$
P_G = \begin{cases} B_E + \mathscr{P}_{\mathscr{G}}^{\max}\dfrac{z}{h_1} & z > h_1 \\[2mm] P_G^{\max}\dfrac{z - h_{ri}}{h_1 - h_{ri}} & z > h_{ri} \end{cases}
\tag{20}
$$

, where B_E is the EBF, $P_G^{\max}$ is the GSP maximum at the depth about $-10\,\mathrm{m}$, and h_1 is the depth of GSP maximum, and $h_r i$ is the Richardson mixing layer.

We also examine whether there is a reliable relationship between the EBF B_E and the GSP maximum $P_G^{\max}$. Fig. 5a is a histogram between between the surface EBF and the maximum GSP on every grid of the SI region, and it shows that grid-by-grid analysis is very noisy and difficult to understand. We regroup the SI grids with levels of surface EBF, and analyses the relation between GSP and EBF by bin-average in each EBF levels. We regroup the horizontal grids in the SI regime to 100 bins in ascending order of the EBF, and calculate bin-averaged GSP vertical profile. Fig. 5b shows the relationship between the EBF and GSP maximum (maximum by larger than 95 % GSP in each vertical profile) after bin-average, which shows that $P_G^{max} = 3B_E$ is an acceptable approximation.

Therefore, at least in this LES simulation by the twelfth day result, the GSP P_G profile could be estimated by

$$
P_G = \begin{cases} B_E\left(1 + 3\dfrac{z}{h_1}\right) & z > h_1 \\[2mm] 3B_E\dfrac{z - h_{ri}}{h_1 - h_{ri}} & z > h_{ri} \end{cases}
\tag{21}
$$

, where B_E is the EBF, h_1 is the depth of the maximum GSP. The calculation of h_1 is undecided, and the scientific implication of the ratio $P_G^{max}/B_E = 3$ is not understood yet. It is unknown whether the ratio is robust for other days during this simulation or for other simulations.

Then we examine the horizontal buoyancy gradient in the SI regions, which are assumed mostly constant over depth by previous studies. Fig. 6 shows the horizontal buoyancy gradient could be taken as a constant value in a layer above $-40\,\mathrm{m}$, a depth of typical convective mixing layer and of buoyancy mixed layer. Below that layer, the horizontal buoyancy gradient change rapidly to the opposite direction. The assumption of constant buoyancy gradient are consistent with the LES truth.

4.3 Momentum Analysis

The GSP profile implies a SI eddy vertical momentum transport possibly leading to a stratified Ekman flow. Fig. 7 shows the SI eddy vertical momentum transport, along with the momentum advection by the mean flow. The momentum advection is small compared to the SI eddy momentum

transport, The overall momentum transport $\mathbf{u}'w' + \mathbf{u}w$ in each direction increases from the surface to a certain depth, and then decrease. The vertical gradient of $\mathbf{u}'w' + \mathbf{u}w$ drives a stratified Ekman velocity; the upper layer's Ekman velocity direction is the opposite direction to the Ekman velocity of the lower layer. However, the velocity in the LES simulation is not stratified.

Therefore, in the momentum budget, there must be some terms compensating the SI eddy turbulent vertical momentum transport $\mathbf{u}'w'$ so that the real velocity is not stratified. Here we try to break down the horizontal velocity by the momentum budget according the Coriolis force. As the SI turbulence scales from $10\,\text{m}$ to $100\,\text{m}$ horizontally, the Reynolds friction stress contributed from turbulence under LES resolution is considered as a separate term not contributed by SI. The total velocity could be understood by

$$
\mathbf{u} = \underbrace{\frac{1}{f}\mathbf{k} \times (\partial_t \mathbf{u} + \mathbf{u}\cdot\nabla\mathbf{u})}_{\text{Inertia velocity}} + \underbrace{\mathbf{u_g}}_{\text{Geostrophic Velocity}} + \underbrace{\frac{1}{f}\mathbf{k} \times \left\langle \partial_{1,2}u'_{1,2}\mathbf{u}' \right\rangle}_{\text{SI Friction by Horizontal Transport } u'_h\mathbf{u}'}
$$

$$
+ \underbrace{\frac{1}{f}\mathbf{k} \times \left\langle \partial_z\mathbf{u}'w'\nabla \right\rangle}_{\text{SI Friction by Vertical Transport } \mathbf{u}'w'} + \underbrace{\frac{1}{f} \times \partial_i \left\langle \tau_{i,j} \right\rangle}_{\text{LES subgrid friction averaged to MITgcm grids}} \tag{22}
$$

$$
\mathbf{u_g} = \frac{1}{f}\mathbf{k} \times \nabla\phi = \int_{\text{bottom}}^{z} \mathrm{d}z\mathbf{1}f\mathbf{k}\times\nabla b \tag{23}
$$

$$
\tag{24}
$$

To simplify the calculation, the LES subgrid friction part is calculated by the difference between the overall velocity and other parts.

Fig. 8b and Fig. 8a show the decomposition of the velocity averaged on the SI regime. The geostrophic velocity and the inertia velocity is small compared to the overall velocity. The velocity is mostly governed by the Ekman velocity contributed by $\mathbf{u}'w'$ and by LES subgrid friction. However, different from previous studies, the Reynolds friction is not only contributed by SI effects, but also by LES subgrid friction averaged to MITgcm grids. The LES subgrid friction is not negligible in calculating the Reynolds friction.

5 Shear Production

Considering the LES subgrid friction would brought an important difference in the TKE budget; the shear production would include LES subgrid friction in the Shear Production, as shown in Eqn. 36

Fig. 9 considers the Shear Production with and without considering LES subgrid friction on SI active grids, compared with the SI turbulent GSP (blue line) and $w'b'$ (red line). It shows the GSP

and $w'b'$ are negligible in TKE budget compared to the Shear Production. The Shear Production with LES subgrid friction (green line) is much greater than the Shear Production only by the SI turbulence (yellow line). Therefore, the LES subgrid friction would be important for TKE budget analysis and for the parameterization scheme based on TKE budget.

6 Conclusion

We examine the Bachman's SI Parameterization in a two ocean front domain. We find that the Bachman's SI Parameterization is not mature enough for studying the SI in regional ocean models. The current SI parameterization could not represent the GSP and $w'b'$ in the LES simulation where SI effects are resolved.

In the comparison between LES simulation and MITgcm with and without Bachman's SI Parameterization. We find that the geostrophic unstable front is more turbulent in LES truth than the MITgcm simulations, and the MITgcm simulations overestimates the vertical buoyancy stratification. What is more, the GSP is not changed significantly by the SI parameterization, as the MITgcm KPP without SI parameterization is similar with SI parameterization, a vertical linear GSP profile thorough z.

On the other hand, the vertical GSP profile of SI regime in the LES simulation is quite different from the Bachman's SI parameterization. The GSP related to the turbulences between $10\,\mathrm{m}$ and $100\,\mathrm{m}$ increases linearly between surface and a depth $-15\,\mathrm{m}$, and then decreases linearly between $-15\,\mathrm{m}$ and the mixing layer bottom.

In this simulation, the baroclinic pressure gradient is small compared to the Reynolds stress and the Coriolis force. The geostrophic velocity is negligible compared to the whole velocity. The velocity is governed by the Ekman balance with Reynolds friction stress, but the Reynolds friction stress consist of not only the SI turbulent vertical momentum transport $\mathbf{u}'w'$ but also of the average of the LES subgrid friction. The subgrid LES friction is as important as the SI turbulent advection in the Reynolds stress, at least in this simulation.

More investigation about the TKE in this two front system is necessary. The linear GSP profile of the Bachman's Parameterization requires one 1-D conservative model that the fluxes inward and outward the SI/GI front would cancelled out each other. However, in this simulation, the flux inward and outward the SI/GI fronts are different. The inward flow are from a geostrophic stable front with cool water and low turbulent kinetic energy, while the outward flow are from the geostrophic unstable front with warm water and high turbulent kinetic energy. Therefore, the fluxes components in the TKE budget would have an effect. The shear production, the proxy for calculating Reynolds stress in the parameterization, is not only influenced by the subgrid dissipation, but also by the energy fluxes inward or outward the SI grids.

Appendix A: From basic momentum equation to PV budget

The Ertel's PV, calculated by the mean flow, is given by

$$q = \boldsymbol{\omega_a} \cdot \nabla b \tag{25}$$

, where absolute viscosity is denoted as $\boldsymbol{\omega_a} = f\mathbf{k} + \nabla \times \mathbf{u}$.

By Eqn. 1 and Eqn. 2, we would have the absolute viscosity and buoyancy governed by

$$\frac{\mathrm{d}\boldsymbol{\omega_a}}{\mathrm{d}t} - \boldsymbol{\omega_a} \cdot \nabla \mathbf{u} = \nabla \times (b\mathbf{k}) + \nabla \times \mathbf{F} \tag{26}$$

$$\frac{\partial b}{\partial t} + \mathbf{u} \cdot b = D \tag{27}$$

$$\nabla \mathbf{u} = 0 \tag{28}$$

Then we could get the governing equation of q by

$$\frac{\partial q}{\partial t} = \frac{\partial \boldsymbol{\omega_a}}{\partial t} \cdot \nabla b + \boldsymbol{\omega_a} \cdot \nabla \frac{\partial b}{\partial t} \tag{29}$$

$$
\begin{aligned}
\mathbf{u} \cdot \nabla q &= (\mathbf{u} \cdot \boldsymbol{\omega_a}) \cdot \nabla b + \boldsymbol{\omega_a}(\mathbf{u} \cdot \nabla) \cdot \nabla b \\
&= (\mathbf{u} \cdot \boldsymbol{\omega_a}) \cdot \nabla b + (\boldsymbol{\omega_a} \cdot \nabla)(\mathbf{u} \cdot \nabla b) - ((\boldsymbol{\omega_a} \cdot \nabla)\mathbf{u}) \cdot \nabla b
\end{aligned} \tag{30}
$$

$$
\begin{aligned}
\frac{\mathrm{d}q}{\mathrm{d}t} &= \frac{\mathrm{d}\boldsymbol{\omega_a}}{\mathrm{d}t} \cdot \nabla b + \boldsymbol{\omega_a} \cdot \nabla \frac{\mathrm{d}b}{\mathrm{d}t} + (\boldsymbol{\omega_a} \cdot \nabla \mathbf{u}) \cdot \nabla b \\
&= (\nabla \times b\mathbf{k} + \nabla \times \mathbf{F})\nabla b + \boldsymbol{\omega_a} \cdot \nabla D \\
&= -\nabla(-\boldsymbol{\omega_a}D + (\nabla b) \times \mathbf{F})
\end{aligned} \tag{31}
$$

However, it is the PV by the mean flow, not exactly the mean PV. The budget of mean PV includes $\mathbf{u}'q'$, a 3rd order momentum uneasy for calculation with the output of MITgcm.

Appendix B: the TKE budget in SI Fronts

The Turbulent Kinetic Energy $E_{TKE} = \langle (u'^2 + v'^2 + w'^2)/2 \rangle$ is the kinetic energy contributed by the turbulent velocity $\mathbf{u}'$, and the turbulent velocity $\mathbf{u}'$ is governed by the LES equations

$$\left(\frac{\partial \mathbf{u} + \mathbf{u}'}{\partial t} + (\mathbf{u} + \mathbf{u}') \cdot \nabla \right)(\mathbf{u} + \mathbf{u}') + f\mathbf{k} \times (\mathbf{u} + \mathbf{u}') = -\nabla(\phi + \phi') + \partial_i \tau_{ij}^{SGS}\mathbf{e_j} + (b + b')\mathbf{k} \tag{32}$$

$$\left(\frac{\partial \mathbf{u} + \mathbf{u}'}{\partial t} + (\mathbf{u} + \mathbf{u}') \cdot \nabla \right)(b + b') = Q \tag{33}$$

$$\nabla \cdot \mathbf{u} = 0 \tag{34}$$

$$\nabla \cdot \mathbf{u}' = 0 \tag{35}$$

, where $\mathbf{u} + \mathbf{u}'$ and $b + b'$ is the full velocity and full buoyancy on each LES grid, the $\mathbf{u}$ and b is the mean velocity and mean buoyancy as the averaged onto the MITgcm grid, $\mathbf{u}'$ and b' is the turbulent part by subtracting the $\mathbf{u}$ and b, τ^{SGS} is the sub-grid LES friction. Then we will have the TKE budget as

$$\frac{\partial E_{TKE}}{\partial t} = -\nabla(\mathbf{u}'\phi') - \nabla(\mathbf{u}E_{TKE}) + \left\langle -u_i'u_j' + \tau_{ij}^{SGS} \right\rangle \partial_j u_i + w'b' - \left\langle \nabla \left(\mathbf{u}' \left(\mathbf{u}' \cdot \mathbf{u}' \right) \right) \right\rangle + \left\langle \partial_i u_j' \tau_{ij}^{SGS} \right\rangle$$
(36)

Sometimes the previous study consider that the pressure gradient part $-\nabla(\mathbf{u}'\phi')$ is the Geostrophic Production with periodic domain and with Ekman Balance.(John R. Taylor and Ferrari 2010) However, in this study, the Symmetric Unstable front is not periodic.

References

Bachman, Scott et al. (2015). *Parameterization of frontal symmetric instabilities. i: Theory for resolved fronts.*

Hamlington, Peter E. et al. (2014). "LangmuirSubmesoscale Interactions: Descriptive Analysis of Multiscale Frontal Spindown Simulations". In: *J. Phys. Oceanogr.* 44.9, pp. 2249–2272. ISSN: 0022-3670. DOI: 10.1175/JPO-D-13-0139.1. URL: http://journals.ametsoc.org/doi/abs/10.1175/JPO-D-13-0139.1 (visited on 09/10/2015).

Hoskins, B. J. (1974). "The role of potential vorticity in symmetric stability and instability". In: *Q.J.R. Meteorol. Soc.* 100.425, pp. 480–482. ISSN: 1477-870X. DOI: 10.1002/qj.49710042520. URL: http://onlinelibrary.wiley.com/doi/10.1002/qj.49710042520/abstract (visited on 03/08/2017).

Hoskins, Brian (2015). "Potential vorticity and the PV perspective". In: *Advances in Atmospheric Sciences* 32.1, pp. 2–9. URL: http://link.springer.com/article/10.1007/s00376-014-0007-8 (visited on 10/07/2015).

Marshall, John C. and A. J. George Nurser (1992). "Fluid Dynamics of Oceanic Thermocline Ventilation". In: *Journal of Physical Oceanography* 22.6, pp. 583–595. ISSN: 0022-3670, 1520-0485. DOI: 10.1175/1520-0485(1992)022<0583:FDOOTV>2.0.CO;2. URL: http://journals.ametsoc.org/doi/abs/10.1175/1520-0485%281992%29022%3C0583%3AFDOOTV%3E2.0.CO%3B2 (visited on 03/08/2017).

Smith, Katherine M., Peter E. Hamlington, and Baylor Fox-Kemper (2016). "Effects of submesoscale turbulence on ocean tracers". In: *J. Geophys. Res. Oceans* 121.1, pp. 908–933. ISSN: 2169-9291. DOI: 10.1002/2015JC011089. URL: http://onlinelibrary.wiley.com.revproxy.brown.edu/doi/10.1002/2015JC011089/abstract (visited on 03/08/2017).

Stone, Peter H. (1966). "On Non-Geostrophic Baroclinic Stability". In: *Journal of the Atmospheric Sciences* 23.4, pp. 390–400. ISSN: 0022-4928, 1520-0469. DOI: 10.1175/1520-0469(1966)023<0390:ONGBS>2.0.CO;2. URL: http://journals.ametsoc.org/doi/abs/10.1175/1520-0469%281966%29023%3C0390%3AONGBS%3E2.0.CO%3B2 (visited on 03/08/2017).

Suzuki, Nobuhiro et al. (2016). "Surface waves affect frontogenesis". In: *J. Geophys. Res. Oceans* 121.5, pp. 3597–3624. ISSN: 2169-9291. DOI: 10.1002/2015JC011563. URL: http://onlinelibrary.wiley.com/doi/10.1002/2015JC011563/abstract (visited on 06/27/2016).

Taylor, John R. and Raffaele Ferrari (2010). "Buoyancy and Wind-Driven Convection at Mixed Layer Density Fronts". In: *J. Phys. Oceanogr.* 40.6, pp. 1222–1242. ISSN: 0022-3670. DOI: 10.1175/2010JPO4365.1. URL: http://journals.ametsoc.org/doi/abs/10.1175/2010JPO4365.1 (visited on 09/10/2015).

Thomas, L. N. and J. R. Taylor (2010). "Reduction of the usable wind-work on the general circulation by forced symmetric instability". In: *Geophys. Res. Lett.* 37.18, p. L18606. ISSN: 1944-8007. DOI: 10.1029/2010GL044680. URL: http://onlinelibrary.wiley.com/doi/10.1029/2010GL044680/abstract (visited on 01/30/2017).

Thomas, Leif N. (2005). "Destruction of Potential Vorticity by Winds". In: *Journal of Physical Oceanography* 35.12, pp. 2457–2466. ISSN: 0022-3670, 1520-0485. DOI: 10.1175/JPO2830.1. URL: http://journals.ametsoc.org/doi/abs/10.1175/JPO2830.1 (visited on 03/08/2017).

Thomas, Leif N. et al. (2013). "Symmetric instability in the Gulf Stream". In: *Deep Sea Research Part II: Topical Studies in Oceanography*. Subtropical Mode Water in the North Atlantic Ocean 91, pp. 96–11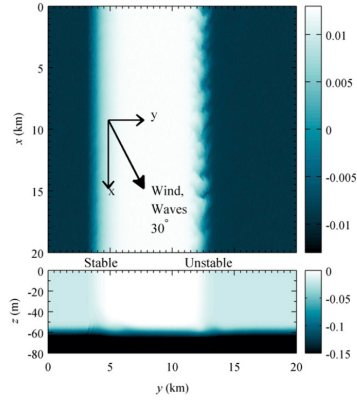0. ISSN: 0967-0645. DOI: 10.1016/j.dsr2.2013.02.025. URL: http://www.sciencedirect.com/science/article/pii/S0967064513000829 (visited on 09/10/2015).

FIG. 1. Temperature field near the beginning of the simulations: (top) $\theta - \langle\theta\rangle_{xy}$ in the x–y plane at the sea surface and (bottom) $\langle\theta\rangle - \theta_0$ as a function of depth in the y–z plane. The left front is stabilized by the Ekman flow (labeled stable) while the right front is destabilized (labeled unstable).

Figure 1: The Temperature Initialization and Wind-Stress for MITgcm and LES simulations, cited from (Hamlington et al. 2014)

(a) LES truth Surface PV (b) MITgcm KPP Surface PV (c) MITgcm SI Surface PV

(d) LES SST (e) MITgcm KPP SST (f) MITgcm SI SST
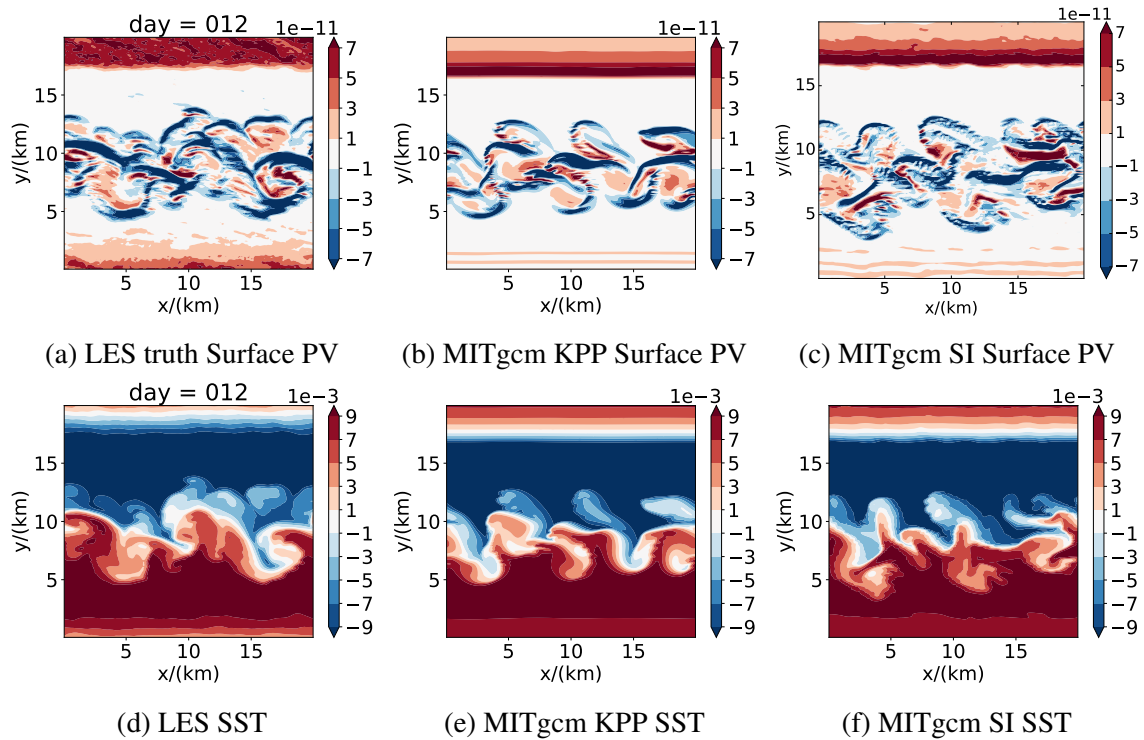
Figure 2: The Surface PV and the Surface Sea Temperature (SST) at the 12th day of LES truth simulation, MITgcm KPP simulation and MITgcm SI simulation. The SST distribution is plotted with subtracting the horizonatal averaged temperature. The upper figures are: 2a the Surface PV of LES truth simulation, 2b the Surface PV of MITgcm KPP simulation, 2c the Surface PV of MITgcm SI simulation. The lower figures are: 3f the SST of LES truth simulation, 2e the SST of MITgcm KPP simulation, 2f the SST of MITgcm SI simulation

17

(a) LES truth Vertical PV

(b) MITgcm KPP Vertical PV

(c) MITgcm SI Vertical PV

(d) LES truth $\Delta\theta = \theta(y,0) - \theta(y,z)$.

(e) MITgcm KPP $\Delta\theta$

(f) MITgcm SI $\Delta\theta$
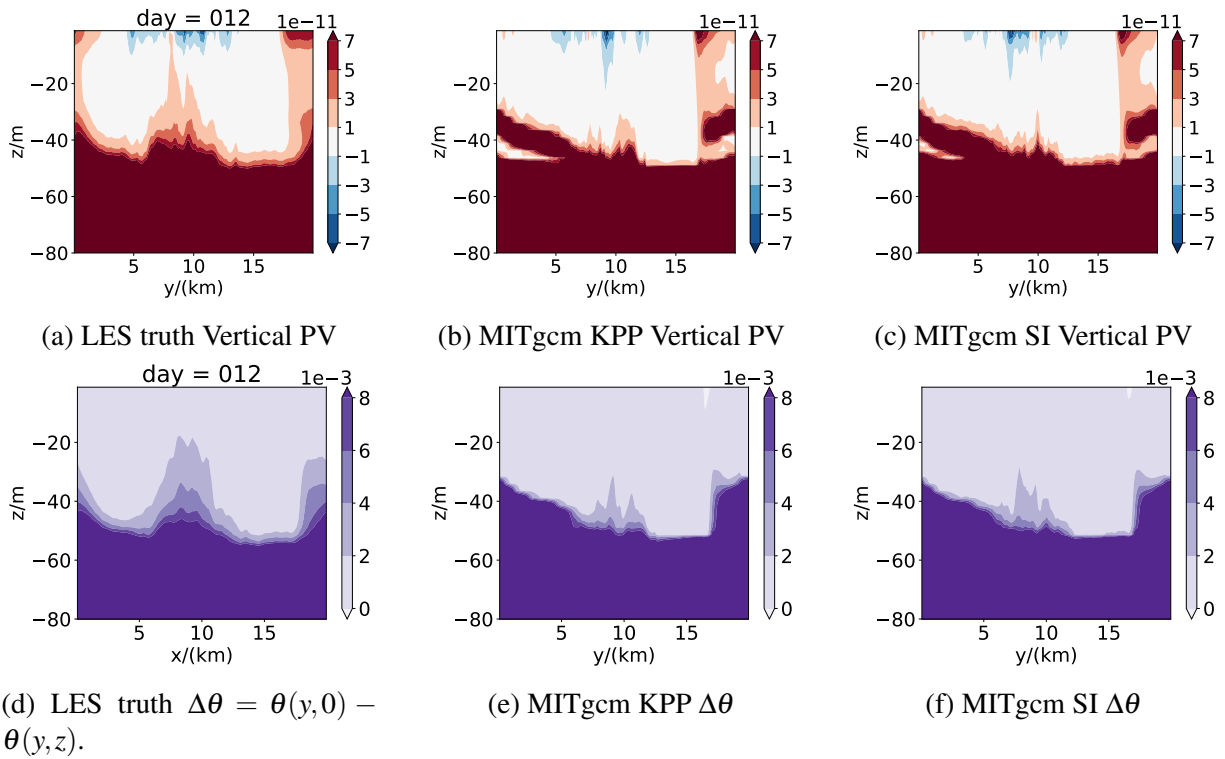
Figure 3: The vertical distribution of PV and of the vertical temperature difference by the SST. The upper figures are x-axis averaged (aligning front averaged) PV, and the lower figures are x-axis averaged vertical temperature difference to the surface. The vertical temperature difference are the potential temperature difference by $\Delta\theta = \theta(y,0) - \theta(y,z)$.

18
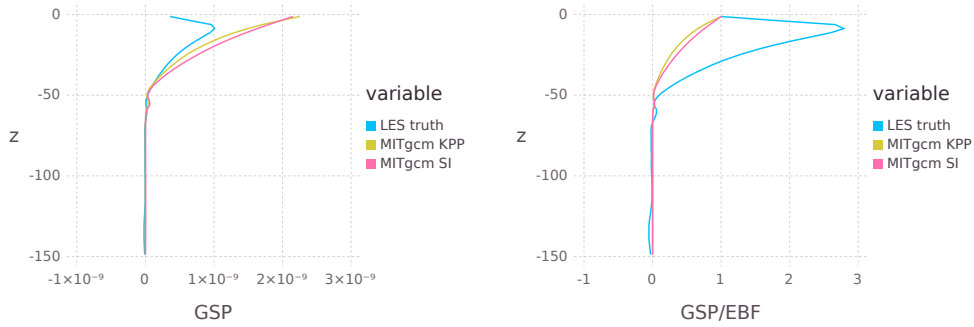
(a) Vertical GSP profile averaged in the SI regime $\langle P_G \rangle_{EBF>0}$

(b) Vertical Profile of the Ratio between averaged GSP and averaged EBF on all SI active grids $\langle P_G \rangle_{EBF>0} / \langle EBF \rangle_{EBF>0}$
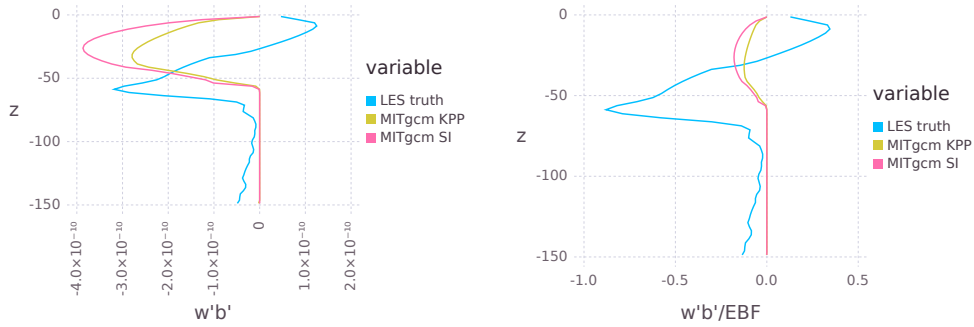
(c) Vertical GSP profile averaged in the SI regime $\langle w'b' \rangle_{EBF>0}$

(d) Vertical Profile of the Ratio between averaged GSP and averaged EBF in the SI regime $\langle w'b' \rangle_{EBF>0} / \langle EBF \rangle_{EBF>0}$

Figure 4: Vertical Profile GSP and $w'b'$ averaged in the SI regimes where EBF is positive. The upper figures are: 4a GSP and 4b GSP per EBF. The lower figures are 4c $w'b'$, $w'b'$ per EBF.
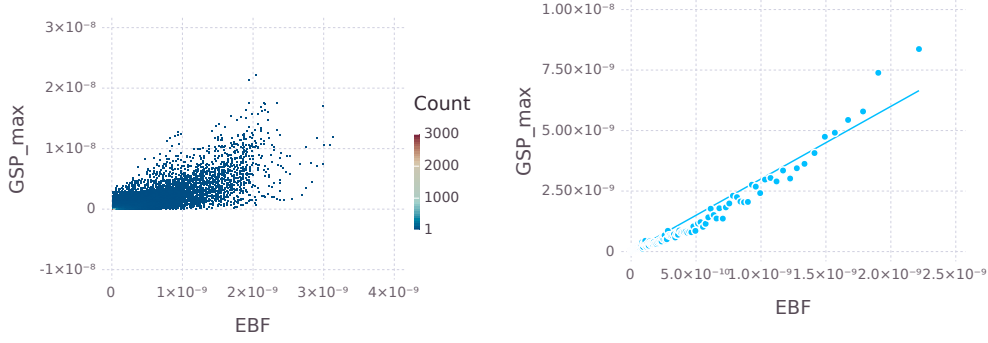
(a) Relation between EBF and Maximum GSP at each grid, 2D histogram

(b) Relation between EBF and Maximum GSP, bin averaged by sorted EBF with 100 horizontal grid in every bin.

Figure 5: GSP Parameters estimation. It is seen that two parameters in GSP vertical profile could be approximated by Surface GSP $P_G = B_E$, where B_E is Ekman Buoyancy Transport, and the Maximum GSP in the tipping point could be approximated by $\mathscr{P}_{\mathscr{E}}^{\max} = 3\mathscr{B}_{\mathscr{E}}$. EBF and GSP are calculated by averaging on and only on SI active grids.
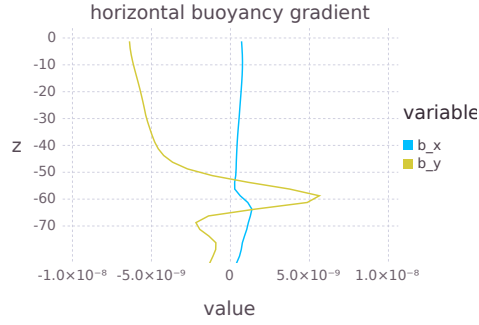

Figure 6: The Horizontal Buoyancy Gradient, $\partial_x b$ and $\partial_y b$, averaged on all SI grids that EBF is positive $B_E > 0$
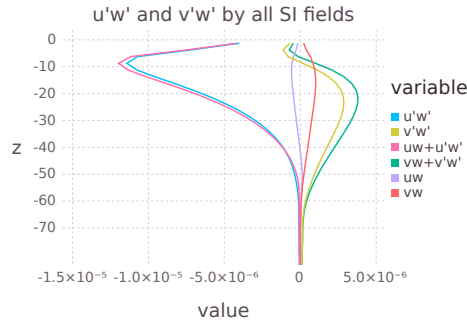

Figure 7: The vertical momentum fluxes averaged on all SI regions, including the SI turbulent part and mean flow advection. $\langle u'w' \rangle$ and $\langle v'w' \rangle$, averaged on SI active grids that EBF is positive $B_E > 0$

(a) Decomposition of the v based on Eqn. 22
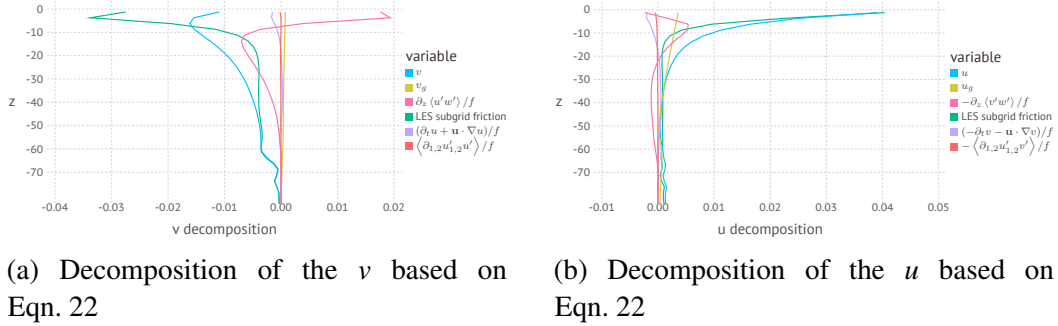
(b) Decomposition of the u based on Eqn. 22

Figure 8: Based on Eqn. 22, the velocity averaged on SI regions are decomposed by the geostrophic velocity, inertia velocity, Ekman velocities by the SI turbulent vertical momentum transport, and by LES subgrid friction. Fig. 8a analyses the x-direction momentum equation and decompose the v velocity, and Fig. 8b analyses the y-direction momentum equation and decompose the u velocity,
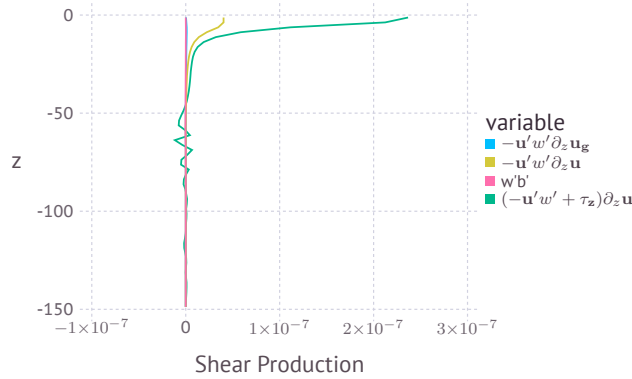

Figure 9: Shear Production Parts in TKE budget: The GSP by SI eddy effects $-\mathbf{u}'w' \cdot \partial_z \mathbf{u_g}$, the SI eddy vertical buoyancy transport $w'b'$, The Shear Production by SI eddy $-\mathbf{u}'w' \cdot \partial_z \mathbf{u}$, The Shear Production by SI eddy and LES subgrid friction $(-\mathbf{u}'w' + \tau_{\mathbf{z}}^{\mathbf{SGS}})\partial_z \mathbf{u}$. All terms are calculated by averaging on all SI active grids